Numerical study of NMR relaxation responses in synthetic clayey sandstone by dual-scale modeling

Yingzhi Cui, *Igor* Shikhov, and *Christoph* Arns*

School of Minerals and Energy Resources Engineering, University of New South Wales, Sydney, Australia

Abstract. Nuclear Magnetic Resonance (NMR) relaxometry is a common technique for petrophysical characterization of sedimentary rocks. The standard interpretation of NMR relaxation response assumes that the fast diffusion limit is valid for the whole pore space, allowing to translate transverse relaxation components into pore apertures. However, porous media naturally exhibit multiple length scales. The diffusion between different sized pores may modify the transverse relaxation rate, weakening the relationship with corresponding pore size populations. Focusing on sandstones, we investigate the impact of diffusion coupling on transverse relaxation depending on kaolinite amount, spatial distribution and temperature. A series of synthetic clayey sandstone models with different clay amounts and morphological distributions (pore-lining, pore-filling and laminated) are generated based on a micro-CT image of an actual Bentheimer sandstone. A dual-scale random walk NMR relaxation simulation with resolved multi-porosity kaolinite models is utilized to avoid problems in near to interface exchange regions typical for effective medium representations. Simulations provide spatially resolved dynamics of magnetization exchange between different porosity populations. The results indicate that increased temperature and kaolinite clay amount with lower micro-porosity allows higher magnetization exchange between micro- and macro-porous regions. Pore-lining clay demonstrates stronger diffusional coupling effects, leading to an overestimation of micro-porosity. We further discuss the impact of diffusion coupling on NMR-estimated permeability via SDR and Coates models.

1 Introduction

Nuclear magnetic resonance (NMR) well logging is an important formation evaluation technique widely utilized for estimation of reservoir petrophysical properties, such as fluid types, saturations, and permeability. The interpretation of NMR data assumes that diffusing protons sample isolated pores (the so-called fast diffusion limit), in which case the observed relaxation rate is related to the surface-to-volume of individual pores [1]. However, molecular diffusion between different pore populations, referred to in literature as diffusional coupling, may lead to erroneous predictions if being unaccounted for. In fact, diffusional coupling appearing as magnetization exchange in NMR data is closely related to the connectivity between micro- and macro-porosity. It has been shown that depending on spatial distribution in rocks, microporosity may be a significant contributor to transport properties and may be responsible for a significant increase of the electrical conductivity [2], higher than anticipated hydraulic flux [3], and may control grain dissolution [4] or wettability alteration through asphaltenes deposition rate. While in this work we focus on the impact of diffusional coupling in the context of NMR interpretation, specifically on the relationship between magnetization exchange and transverse relaxation (T_2), the developed analysis is applicable to all mentioned transport problems.

The diffusional coupling phenomenon in respect to NMR data analysis has been extensively studied in synthetic porous media [5, 6], or sedimentary rocks, namely carbonate [7 - 10] and shaly sandstone [6, 11]. It has been reported in literature that two key petrophysical properties estimated from T_2 responses (irreducible water saturation and permeability) are affected if magnetization exchange between distinctive pore populations is significant. The standard practice in NMR core analysis is to relate T_2 values to pore size, i.e. the short relaxation time components of the T_2 distribution can be attributed to irreducible or capillary bound water (CBW), while the longer time components separated by the cutoff value ($T_{2,cutoff}$) correspond to mobile fluid in larger pores (known also as free fluid index FFI) [12]. However, it was demonstrated that calculated BVI values from NMR T_2 responses of sedimentary rocks exhibiting a well-coupled pore system are prone to large errors approaching 50% [15]. Interestingly, it was observed that at high temperature these effects were far less severe than at ambient temperature. The exact reason of this observation was not established since temperature dependence of governing physical properties (increase of self-diffusion coefficient of fluids and surface relaxivity [16]) suggests exactly the opposite. It is fair to acknowledge the limitation of the numerical simulation model used by [15], excluding internal field gradients effects from consideration. In addition, the temperature dependence of surface relaxivity is still poorly understood – both increases and decreases with temperature are reported in literature [6]. In the case of complete coupling, the micro- and macro-pores cannot even be identified from T_2 distribution resulting in the erroneous estimation of irreducible saturation [11].

NMR based permeability is estimated using one of two correlations: T_{2lm} - based SDR equation (after Schlumberger

* Corresponding author: c.arns@unsw.edu.au

Doll Research) [17] and $T_{2,cutoff}$ - based Coates model [18]. The magnetization exchange tends to shift one of the two coupled components – the one having a longer relaxation time – towards a shorter relaxation time [19], affecting NMR-related components of both models (T_{2lm}, CBW/FFI) and creating poor estimates. For instance, [8] demonstrated that permeability estimations based on SDR model for different rocks could exhibit relative errors up to 15%. [20] shows that T_2 shifts to shorter times because of intermediate diffusion coupling between micro- and macro-pores in chlorite-coated sample leading to inaccurate permeability estimation. In addition, a pore-connectivity parameter, introduced for the Coates model, offers more precise permeability and movable fluid volume estimates in complex coupled pore geometry [21]. The study [22] further extended to directional pore-connectivity factor to accurately characterize anisotropic directional permeability of sedimentary rock with NMR measurements.

Numerically diffusional coupling was analyzed in the context of relaxation in ideal pore networks [23]. Three geometrical models were presented to describe magnetization decay in carbonates with mixed intra- and intergranular porosity [24]. They reported that diffusional coupling may causes a shift of the longer relaxation peak and distort the amplitudes of the T_2 distributions. [7] further investigated coupling effects based on a 3D sphere model; constant internal magnetic gradient assumed. The results indicate that inter-pore diffusion has a strong impact on NMR measurements. More recently, simulations based on 3D periodic micro-porous grain consolidation models support the interpretation of NMR measurements in terms of magnetization exchange between dual-scale pore system [25 - 27]. The simplified models miss the morphological and geometrical information of the sedimentary rocks. To have an explicit representation of porous media, the X-ray micro-CT tomography was employed. Pore-pore coupling was analyzed by tracking random walkers within the partitioned pore space, which demonstrates that diffusion between pores occurs to a significant degree [28]. A numerical study on fractured carbonates [29] established that diffusional coupling may lead to underestimation of intergranular porosity by more than 10%. Although micro-CT images can offer more accurate internal structures of rock, micro-porosity often cannot be fully resolved due to either resolution limitations or simultaneous requirements of resolution and field of view. The non-resolved intermediate phase is then treated either as effective medium [28] or merged into the solid phase [30]. Yet, scanning electron microscopy (SEM) micrographs even of relatively simple rocks like Bentheimer sandstone (Fig. 1) indicate that the realistic micro-structure is complicated. Clay particles may fully or partially fill the pore space with heterogeneous local micro-porosity for each clay pocket. More generally, clay may also coat solid grains or appear as thin laminations [31]. These differences in the spatial distribution of clay as well as varying clay porosity and connectivity invite more complex coupling effects.

In this work we consider the impact of the spatial distribution and amount of clay on NMR relaxation responses. A simulation-based methodology is employed, which enables the quantification of the diffusional coupling phenomenon, in particular the evolution of magnetization across clay interface and impact on NMR relaxation derived

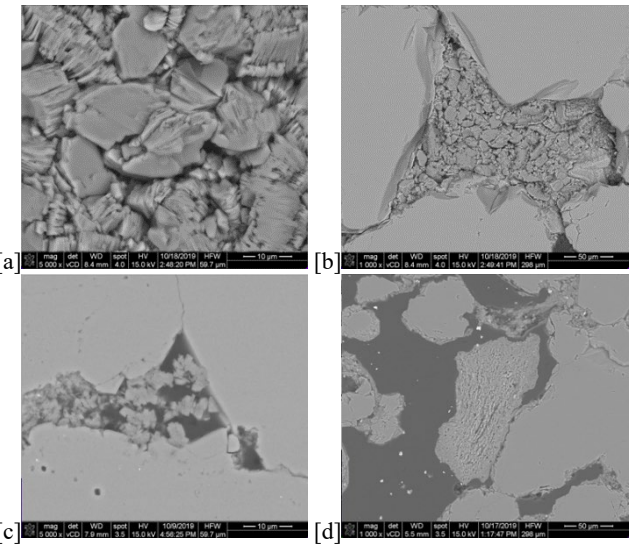

Fig. 1. [a] SEM image of kaolinite pocket in Bentheimer Sandstone; [b] Low porosity full-filled kaolinite pocket. [c] Medium porosity partial-filled kaolinite pocket. [d] Coated clay around quartz.

petrophysical properties such as irreducible water saturation (BVI) and permeability. A series of synthetic clayey sandstone models are generated with different clay amounts (6 vol% - 16 vol%) and synthetic morphological distributions (loosely termed coated, laminated, pore-lining and pore-filling) combined with resolved multi-porosity kaolinite models to track magnetization exchange between macro- and micro-pores. The evolution of magnetization exchange between different porosity populations is captured as function of observation time and penetration depth, together with the increase in the diffusion coefficient due to temperature; other intrinsic physical parameters like mineral-specific surface relaxivities are set constant in this fundamental study. Accounting for these effects from clay consequently improves NMR-estimated permeability via SDR and Coates models and enables more robust petrophysical interpretations.

2 Methodology

The objectives of this study require generation of clay distributions at different scales ranging from dispersed (pore-lining and pore-filling) to coated and laminated clay types. In the following we first introduce the methods for the coarse-scale distribution of clay regions, followed by fine-scale clay structure modeling, associated NMR simulations, and regional analysis fields embedded in the NMR solver enabling the local tracking of magnetization exchange. This is followed by a recapturing of NMR permeability correlations and the determination of permeability from tomographic images using the lattice Boltzmann technique.

2.1 Synthetic Clayey Sandstone

The synthetic clayey sandstones 3D models utilized in this study are based on the micro-CT image of Bentheimer sandstone shown in Fig. 2 and the SEM images (Fig. 1). The latter shows that pores of the original rock can be either fully or partially filled with kaolinite aggregates. Furthermore, those clay pockets exhibit different aggregate density and

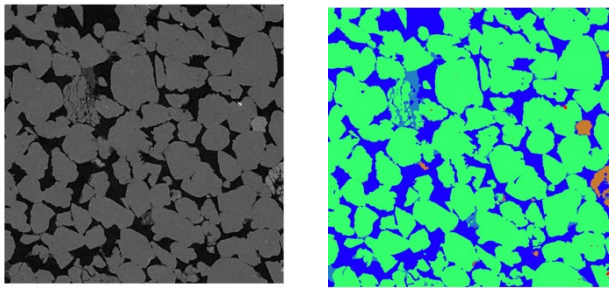

[a] [b]

Fig. 2. [a] Slice through an 800^3 subdomain of a tomogram of Bentheimer sandstone at a resolution of 2.2 μm voxel and [b] corresponding five phase segmentation. The colors are: dark blue - pore, green - quartz, cyan - clay, brown - feldspar, red - high-density minerals.

thus clay region porosity. This translates to clay regions with different intensity in the micro-CT images, where clay particles are not resolved (Fig. 2a). It is assumed that the intensity of kaolinite particles is similar to quartz. Therefore, the intensity in each clay region (I_c) is volume-weighted by the pore intensity (I_p) and quartz intensity (I_q). The intensity distribution of clay pockets (Fig. 3a) shows that the major values are around 1.2×10^4 to 1.3×10^4. The porosity of each clay pocket is estimated by $\phi_k = (I_q - I_c)/(I_q - I_p)$. The corresponding distribution shows that clay region porosity falls mainly into the range of 0.3 - 0.6 (Fig 3b). Consequently, we allowed for four discrete clay porosity labels corresponding to clay porosity of $\phi_c \in \{0.3, 0.4, 0.5, 0.6\}$.

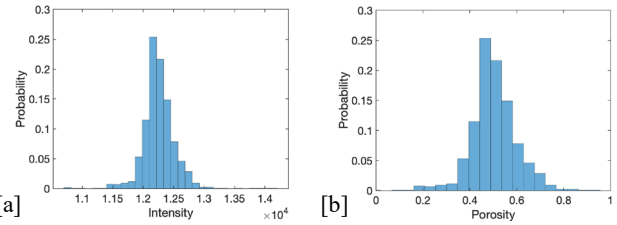

[a] [b]

Fig. 3. [a] Intensity probability distribution of all clay pockets in the Bentheimer micro-CT images; [b] corresponding porosity distribution of clay pockets.

Four different clay distributions are constructed: pore-filling, pore-lining, coated and laminated. The models are generated with different clay volume fractions of 6 vol%, 11 vol% and 16 vol% to investigate the effects from clay amount. For pore-filling clay pockets we divided the resolved pore space into convex regions or pores. This is achieved by performing a watershed transformation [33] on the Euclidean distance map [34, 35] (Fig. 4a). We randomly assign the clay phase to the partitioned pores until the clay volume fraction meets the requirement. For pore-lining clay pockets, we determine the center for each pore (Fig. 4b) and preserve the pore fraction corresponding to the maximal inscribed sphere as pore space.

The remaining pore space is assigned as clay, resulting in a partial-filled clay layer of varying thickness. The coated clay phase is assigned only based on the distance threshold of EDT map. For laminated clay, we generated different layered system according to kriging interpolation method with random range, sill, and nuggets for mimicking the clay distribution.

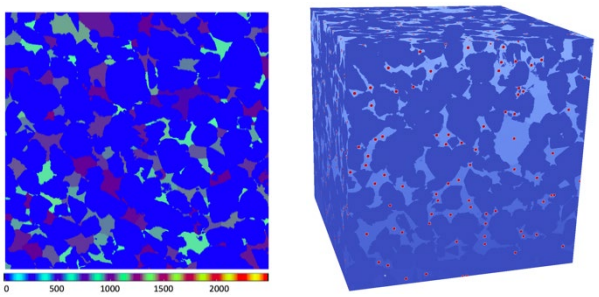

[a] [b]

Fig. 4. [a] Slice through the 800^3 watershed pore partitioning – region boundaries are the watersheds of the EDT, and [b] a 3D visualization of the centers in 800^3 watershed pore partitioning. Resolution: 2.2 μm/voxel.

To satisfy the clay volume fraction, the mean thickness values of each horizon are different. To reduce discretization effects from the image and force an accurate calculation of the internal magnetic fields [32], a tri-linear interpolation is applied with factor 4 refinement. Thus, the original 800^3 domain is refined to 3200^3 voxels with voxel size of 0.55 μm/voxel and smoother solid surface shown in Fig 5.

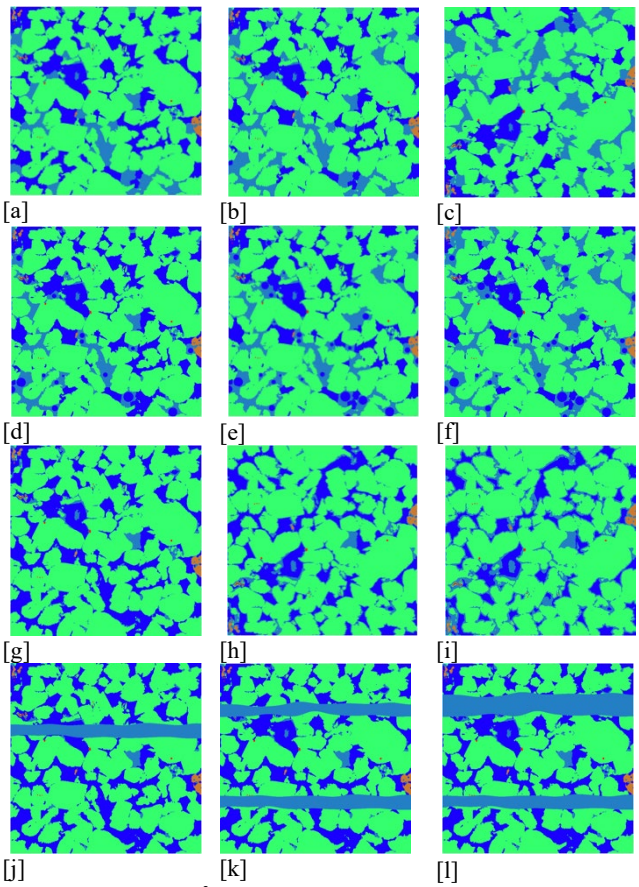

[a] [b] [c]
[d] [e] [f]
[g] [h] [i]
[j] [k] [l]

Fig. 5. Slices of 3200^3 synthetic clayey sandstone (resolution 0.55 µm/voxel). [a-c] pore-filling clay; [d-f]: pore-lining clay; [g-i]: coated clay; [j-l]: laminated clay. The left column with 6 vol% clay phase, the middle column with 11 vol% clay phase and the right column with 16 vol% clay phase. The colors are: dark blue - pore, green - quartz, cyan - clay, brown - feldspar, red - high-density minerals.

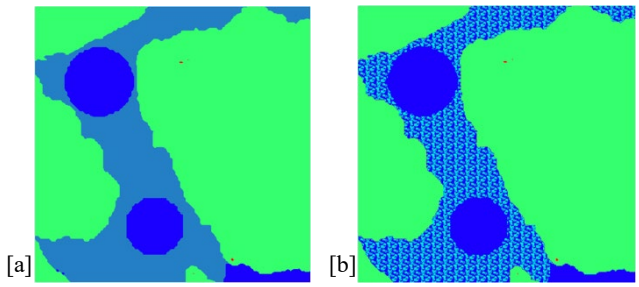

Fig 6. [a] A 400^2 subsection of the 3200^3 synthetic clayey sandstone (16 vol%) with unresolved clay phase and voxel size of 0.55 μm. [b] Corresponding 10000^2 cross-section of [a] where each clay pocket is replaced by the corresponding kaolinite model. The resolution of the fully resolved model is 22 nm/voxel. The color schemes is: dark blue - pore, green - quartz, cyan - clay, brown - feldspar, red - high-density minerals.

2.2 Kaolinite Model

Kaolinite is one of the most common clay mineral constituents of sedimentary rocks, especially in sandstones. However, the microstructure cannot be fully resolved in the micro-CT image due to resolution limitations (Fig. 2). To resolve the microstructure within kaolinite pockets, we reconstruct 3D volumetric kaolinite models following the method detailed in [36]. In this study, we discretize the kaolinite microstructure as a periodic domain of 400^3 voxel with resolution of 22 nm, which is 1/100 of micro-CT image resolution. Four realizations with average porosity $\phi_c \in \{0.3, 0.4, 0.5, 0.6\}$ are constructed. Surface area S_v and T_{2eff} of the clay models are reported in Table 1 and are in agreement with published surface area measurements [6, 37] and T_2 values [38]. Here, the density for kaolinite we used is 2.6 g/cm^3. The surface relaxivity (ρ_2) is 1.2 μm/s. For NMR simulations the unresolved clay regions of the micro-CT images are replaced by the corresponding kaolinite model according to clay porosity. Fig. 6 depicts a subsection of the coarse scale model with unresolved clay regions, and the corresponding high-resolution model with fully resolved structure and different clay pocket porosity.

Table 1. Surface area (S_v) and effective relaxation time (T_{2eff}) of different porosity kaolinite model.

ϕ_c	S_v (m^2/g)	T_{2eff} (ms)
0.3	23.5	13.2
0.4	19.7	18.7
0.5	15.1	24.5
0.6	12.3	30.3

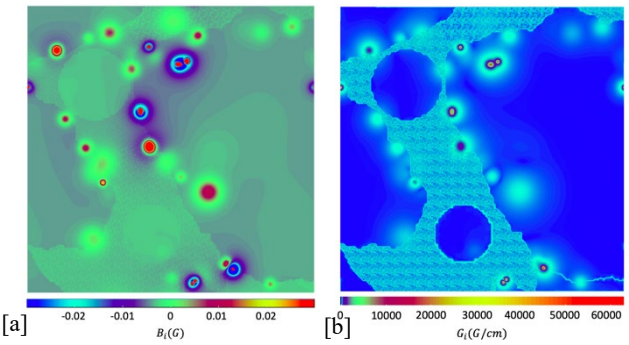

Fig 7. Cross-section of Fig 6 corresponding 10000^2 subset of [a] internal magnetic field distribution $B_i(\mathbf{r})$ and [b] internal magnetic gradient distribution $G_{in}(\mathbf{r})$ at 22 nm/voxel.

2.3 Dual-scale NMR Relaxation Simulation

The dual-scale NMR relaxation response simulation has been described in detail previously [32]. In this work the simulation approach is extended to clay regions with different porosity. Furthermore, we implement the tracking of magnetization for dual-scale simulations, following the approach of [39]. In the previous section we detailed our approach of combining the resolved clay regions with the micro-CT based segmented tomogram. This resulted in a micro-structure where the interpolated coarse-scale segmentation (0.55μm resolution) is mapped to a voxel size of 22nm, the same as the clay region models. Thus, a random walk could now in principle be carried out completely in the resolved pore space. However, for the simulation of the NMR transverse relaxation response the internal magnetic field at every location is required. The calculation of high-resolution internal magnetic fields (B_i) is achieved by a separation of near- and far-field effects in a dipole-approximation of the internal field with dual-scale samples [32]. This allows calculating the coarse-scale internal magnetic fields via Fourier methods. The fine-scale internal magnetic fields of the periodic clay models are calculated separately. Then, the fine resolution internal magnetic field can be calculated as a combination of the coarse scale field interpolated to a voxel size of 22nm and a perturbation from the fine-scale field. The latter is calculated by deducting the coarse scale trend from the fine-scale fields (ensuring zero mean at tomogram scale). Like the fine-scale microstructure, B_i is never stored in memory at full resolution (at $80{,}000^3$ voxel it would be prohibitively large) but constructed locally when required for either a random trajectory during NMR simulations, to visualize parts of the high-resolution internal magnetic field, or to extract statistics. An example of high-resolution B_i distribution and corresponding spatial internal gradient distribution (G_i) is shown in Fig. 7.

Once the magnetic field distribution is generated, the random walk algorithm is carried out on a regular cubic lattice with fine-scale resolution (ϵ = 22 nm). The corresponding time step τ_i of a step i is given by $\tau_i = 6D_0/\epsilon^2$, where D_0 is the free diffusion coefficient of water, which we here vary with temperature. Bulk and surface relaxation are implemented as signal weighting factors for each step, with $S_i = S_b S_s$. Here $S_b = \exp(-\tau_i/T_{2,b})$ is the contribution by bulk relaxation, and $S_s = 1 - 6\rho_2\tau_i/(\epsilon A)$ the contribution by surface relaxation, where ρ_2 is the surface relaxivity of solid. For steps within the same fluid $S_s = 1$. A is a correction

factor of order 1, which accounts for the details of the random walk implementation [40]. For imaged structures, this value is typically close to A = 3/2. Besides, the contribution of the internal field to dephasing is calculated explicitly written as $\Delta\phi$. The bulk relaxation, surface relaxation and phase variation caused by diffusive relaxation are then incorporated into the calculation of each walker's magnetization, which becomes

$$M_w(t_j) = M_w(0)\cos\left[\Delta\phi(t_j)\right]\prod S_i \qquad (1)$$

Averaging over random walks and recording at $t = nt_E$ (n= 1,2,...N) results in the magnetization decay M(t). The relaxation time distribution is obtained by fitting a multi-exponential decay to M(t).

In this study, the NMR transverse relaxation response is simulated for a given Larmor frequency of f = 2MHz and echo time t_E = 200 μs. For synthetic clayey sandstone, the surface relaxivity ρ_2 of the solid and the magnetic susceptibility χ of each phase are reported in Table 2.

Table 2. The surface relaxivity (ρ_2) and magnetic susceptibility (χ) of each phase assigned for NMR relaxation response simulation.

Phase	ρ_2 ($\mu m/s$)	χ (μSI)
Water	-	-8.9
Kaolinite	1.2	-11.0
Quartz	9.0	-12.0
Feldspar	9.0	-12.0
High-Density	60.0	5270

2.4 EDT Based Regional Magnetization Exchange

The magnetization exchange (or coupling) refers to a fraction of the spin population, which originates in one of the porosity types (e.g. macro-porosity) at the beginning of NMR signal acquisition, and found after a specific time interval (exchange time) in another porosity type (e.g. micro-porosity). The spin population in question should possess a measurable magnetization, thus defining a process sensitive to porosity types morphology and inter-connectivity.

Measuring the magnetization exchange between porosity partitions using random walk simulations is achieved by adding a phase label to the start and end positions of the walkers and employing the Euclidean distance transform (EDT). The former labeled phase can identify the diffusion of magnetization as macro-micro (start at macro-pore and end at micro-pore) and micro-macro (start at micro-pore and end at macro-pore). The latter EDT refers to a process that generates Euclidean distance fields for a 3D voxelized representation of samples. Valid distance values for each phase are calculated by assigning each voxel of the phase of interest the shortest distance to a voxel of another phase using distances between voxel centers. The implementation is a parallel version of algorithm 4 of [34]. An example of high-resolution EDT maps for macro- and micro-porous regions is depicted in Fig. 8. Given the distance information and phase labels, the quantification of the local magnetization evolution can now

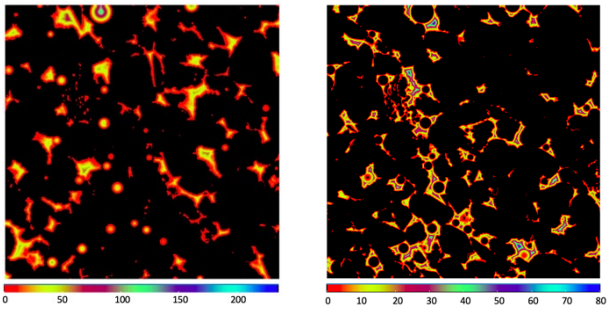

[a] [b]

Fig 8. A slice of Fig 5 [e] corresponding high-resolution EDT map for [a] macro-pores in voxel unit, 3200^2 in 0.55 μm/voxel; [b] micro-pores in voxel unit, 3200^2 in 0.55 μm/voxel.

be achieved by counting the walker strength in respect to a particular shell and phase. This information allows tracking the penetration depth (d) of magnetization diffusing across different pore populations. In addition, the magnetization exchange is counted at different observation time $t = nt_E$ (n= 1,2,...N). Therefore, The magnetization exchange can be characterized as a function of penetration depth and observation time $M_{ex}(d,t)$.

2.5 Permeability Estimation

In this section we briefly overview common NMR permeability correlations as well as the lattice Boltzmann technique to calculate permeability directly from tomographic images. Together these techniques are utilized to quantify the effect of clay content and spatial distributions with associated diffusion coupling on permeability predictions.

2.5.1 NMR Correlated Permeability Model

The NMR-estimated permeability by SDR [17] and the Coates models [18] are given by the following equations

$$k_{SDR} = a_s \phi^b T_{2lm}^c \qquad (2)$$

$$k_{Coates} = a_c \phi^b \left(\frac{FFI}{BIV}\right)^c \qquad (3)$$

where k is permeability in μm^2 (approx. mD), ϕ is porosity in %, with b and c exponents typically set to 4 and 2, respectively. For the SDR model (Eqn. 2), a_s is a parameter accounting for formation lithology. The SDR estimates mean hydraulic radius through the logarithmic mean relaxation time T_{2lm} and despite apparent limitations has proven applicable to fully water saturated water-wet formations. For the Coates Model (Eqn. 3), a_c is the Coates permeability coefficient, which is often used as denominator of porosity. The fixed $T_{2,cutoff}$ divides the T_2 distribution into two fractions corresponding to bound water (BVI, shorter relaxation times) and free fluid (FFI, longer relaxation times). Generally, cut-off times of 33 ms and 92 ms are appropriate for sandstones and carbonates, respectively [18]. However, our previous study shows that $T_{2,cutoff}$ values determined based on the irreducible water saturations S_{wirr} vary in different sandstones [36]. The primary assumption behind these correlations is that the fast diffusion limit condition applies to all components of the relaxation spectrum.

The SDR correlation is essentially based on a general relationship between permeability k, characteristic length scale of a pore system L, and porosity ϕ, $k \propto \phi^m L^2$, reported by many authors [41 - 43]. We note that the definitions of the characteristic length scale are different. L can be obtained from capillary pressure measurements in the study [41]. On the other hand, L is defined as dynamically connected pore size in the study from [42]. While the length scale offered from NMR T_2 distribution is related to pore volume-to-surface ratio V_p/S. $k \propto \phi^{1.8}(V_p/S)^2$ for the grain consolidation model is presented in [43]. More recently, the correlation between permeability and four different types of pore diameters is demonstrated as $k \propto \phi^4\langle d\rangle^2$ based on micro-CT image [35]. Eqn. 2 can be easily expressed in the latter form noting in the fast diffusion limit $T_2 \sim L/(6\rho)$. Since the observable physical property is relaxation time and numerical simulation offers (and requires as input) surface relaxivity, we apply the squared proportionality factor 6ρ to the lithological parameter a_s, making it dimensionless: $a_s' = a_s/(6\rho)^2$. Typically, in laboratory core analysis the only unknown in the SDR equation is the lithological parameter, which has to be established for log calibration. Below we discuss the effect caused by the diffusional coupling in presence of different amount of clay on the modified lithological parameter a_s'.

2.5.2 Lattice Boltzmann Method

The Lattice Boltzmann Method (LBM) is a mesoscopic approach to fluid mechanics utilizing particle densities via a collision and streaming algorithm. The LBM has become an effective method for estimation of fluid flow in porous media because of its simplicity and flexibility to various flow geometries [44 - 46]. It is employed in this study to provide reference permeability values evaluate the enhancements in the NMR permeability estimations. The fluid is treated as continuous medium, and the solution of a discretized Boltzmann equation can match the Navier-Stokes equation. The D3Q19 (3-dimensional lattice with 19 possible velocity directions) lattice [47] is selected. The method starts with the initialization of distribution functions. The macroscopic fluid properties can be computed by

$$\rho(\boldsymbol{x}, t) = \sum_{i=1}^{19} f_i(\boldsymbol{x}, t) \qquad (4)$$

$$\rho\boldsymbol{v}(\boldsymbol{x}, t) = \sum_{i=1}^{19} \boldsymbol{e}_i f_i(\boldsymbol{x}, t) \qquad (5)$$

where ρ is the macroscopic fluid density, $\boldsymbol{v}$ is the velocity, $\boldsymbol{e}_i$ are the microscopic velocity vectors and f_i is the particle density distribution function. After applying boundary conditions, the algorithm for density evolution which includes the stream and collide operation is given by

$$f_i(\boldsymbol{x} + \boldsymbol{e}_i\delta t, t + \delta t) = f_i(\boldsymbol{x}, t) - \frac{f_i(x,t) - f_i^{eq}(x,t)}{\tau} \qquad (6)$$

where f_i^{eq} is the equilibrium distribution function and τ is the relaxation time. In the simulation, the BGK (Bhatnagar-Gross-Crook) collision kernel is applied to simulate the single phase fluid behavior with bounce-back condition at the fluid-solid interface [48] The pressure gradient is simulated by a body force [46].

3 Magnetization Exchange Analysis

In this section we analyze the exchange of magnetization between different compartments of the clayey sandstone samples as function of clay distribution, clay region porosity, and temperature. Change in those parameters affects the main observables, namely the shape of the T_2 distribution, the position of individual modes of the distribution, as well as the size of the spatial regions active in magnetization exchange, which are discussed in the following. Consequences for permeability estimation are analyzed in the section thereafter.

3.1 Clay Distribution and Micro-porosity Effects

Consider first the relationships between diffusional coupling, clay distribution, clay content, and clay region porosity (ϕ_c) at ambient conditions. NMR simulations were conducted on both the pore-lining and pore-filling samples for a range of clay fractions, where kaolinite clay models with constant porosity ϕ_c (average over the 400^3 clay model) are mapped to the respective clay regions. The corresponding T_2 distributions are given in Fig. 9. Stronger diffusional coupling effects can be observed for the coated and pore-lining clay distributions with higher clay porosity (ϕ_c). The part of the T_2 distribution associated with coated type of clay morphology exhibits faster relaxation time than other three clay morphology despite equal volumetric fraction in sandstone. Especially, with increasing clay amount, the T_2 distribution of the coated clay becomes unimodal and no longer represents pore size distribution. Diffusional coupling enhanced the relaxation rate and the slow relaxation time peak shifts to short time.

The correlation between clay amount and the transverse relaxation rate ($1/T_{2lm}$) is demonstrated in Fig. 10. $1/T_{2lm}$ of four clay morphological types demonstrate a linear relationship with clay content in different slopes. The micro-porosity has more impact on the relaxation rate of grain-coating and pore-lining clay morphology when the amount surpasses 10 vol% (Fig 10 [b, c]). The higher clay porosity and stronger coupling effects lead to the fast relaxation peak shifts for the longer relaxation times, resulting in a decreased slope and vice versa. The distortion of relative amplitudes of the fast relaxation peak and slow relaxation peak due to diffusional coupling may break down the correlation between the peak area ratio and the porosity fraction of micro-pores and macro-pores [24]. The micro-porosity may be overestimated with increasing clay amount. We note that both grain-coating and pore-lining clay morphological types with higher clay porosity exhibit larger errors. This is because of two effects -- the higher clay porosity (ϕ_c) allows more protons to diffuse between micro- and macro-pores and the pore-lining clay distribution pattern offers more clay-region to macro-pore interface area and thus lead to a higher diffusion

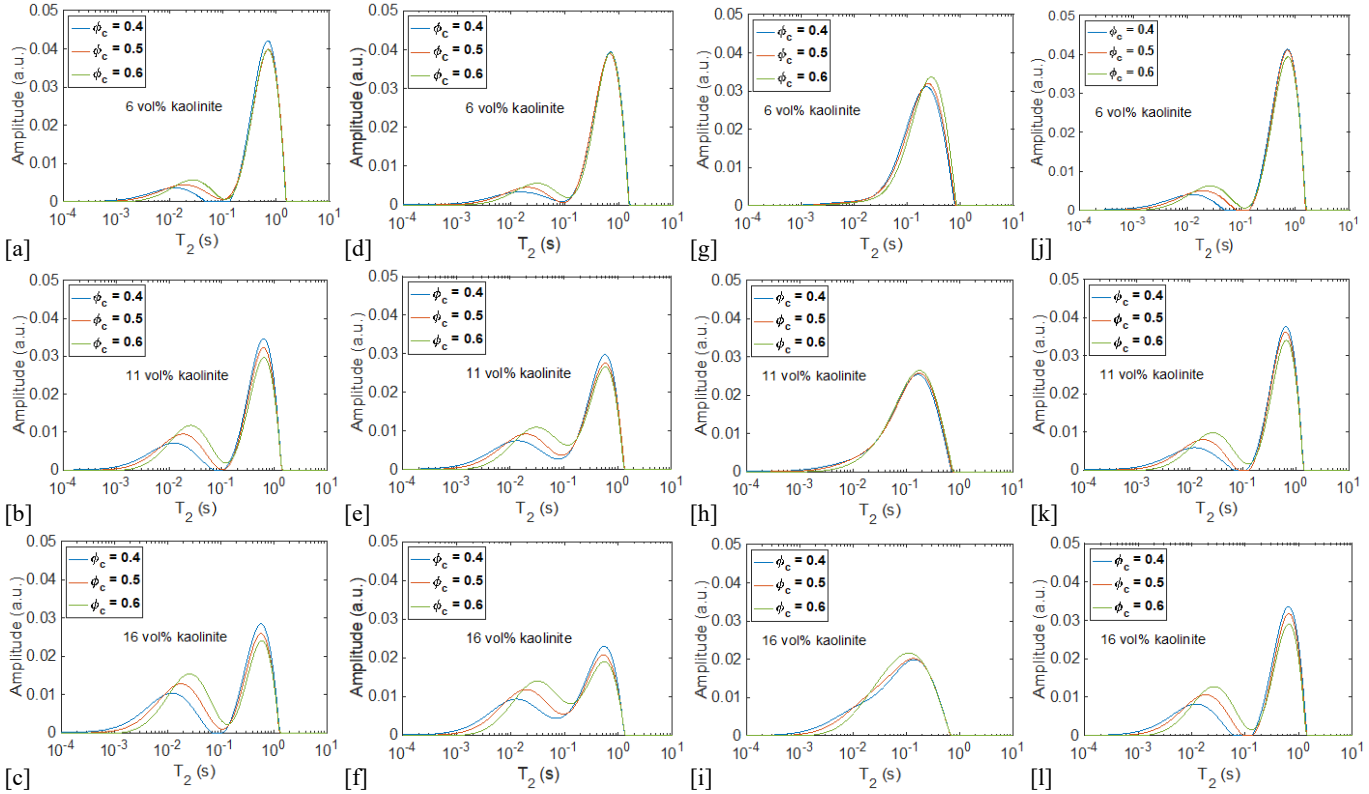

Fig. 9 The T_2 distribution of [a-c] pore-filling; [d-f] pore-lining; [g-i] coated; [j-l] laminated synthetic sandstone with different clay amount. *Top row:* 6 vol%, *middle:* 11 vol%, *bottom:* 16 vol%. $\phi_c \in \{0.4,0.5,0.6\}$ denotes the micro-porosity of kaolinite

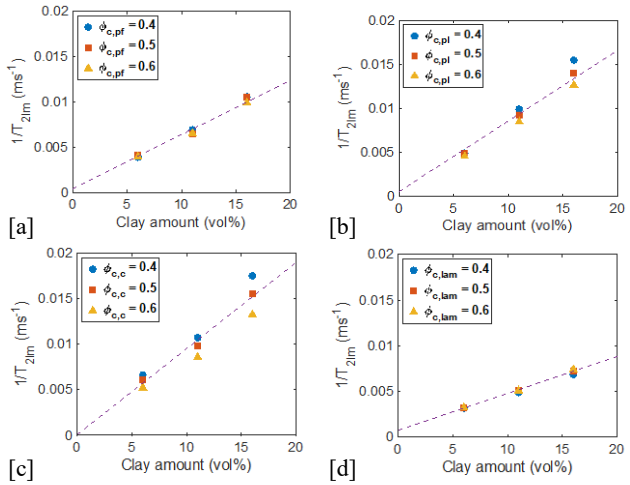

Fig. 10 Linear relationship between clay volume fraction and T_{2lm} for different clay distributions. [a] pore-filling, [b] pore-lining, [c] coated, [d] laminated. The purple dashed lines are the linear trend between T_{2lm} and clay amount.

3.2 Diffusional Exchange Between Different Compartments

We demonstrate the correlation between magnetization exchange (M_{ex}(d,t)) and time as well as Euclidean distance. Since the samples containing different clay amounts indicate the same trends, we chose a system with 11 vol% clay amounts as a representative example. M_{ex}(d,t) as function of observation time is shown in Fig. 11, where $\sum d$ is the distance integration over each EDT shell. Similar magnetization exchange profiles are presented in both macro-micro and micro-macro directions. At the beginning, a growing number of walkers diffuse between micro- and macro-porous regions with time increasing. The diffusional exchange of magnetization reaches a maximum value at around 10-30 ms. After that, magnetization exchange decreases and there is almost no leaked magnetization between two pore populations when time exceeds 1s as defined by compartment association at start and end position of the exchanging spin packet. The magnetization exchange is significantly affected by micro-porosity for coated and pore-lining clay morphology when diffusion occurred in both two directions. These two clay distribution patterns with higher micro-porosity allow protons diffusing between micro- and macro-pores more frequently. For grain-coated morphological pattern, the magnetization exchange when $\phi_c = 0.6$ is two times stronger than $\phi_c = 0.4$. While, the $M_{ex}(\sum d,t)$ for pore-filling and laminated samples are much closer. Overall, the coated clay type exhibits five times higher magnetization exchange compared to other samples. The magnetization exchange of pore-lining clay type demonstrates two-fold compared to pore-filling and laminated one when clay porosity is 0.5 and 0.6. However, if porosity of the compared clay types reduced to 0.4, the difference in exchanged magnetization diminishes. This can be explained by stronger surface relaxation in the clay region due to an increase in surface-to-volume ratio.

Consider now the correlations between magnetization exchange and Euclidean distance presented in Fig 12. Here, we take examples of pore-filling and pore-lining samples. The overall trend demonstrates that magnetization exchange presents approximately exponential decay with Euclidean distance for both directions. The leaked magnetization from two porosity populations towards the other is reduced as the walkers moving far from the interface boundary.

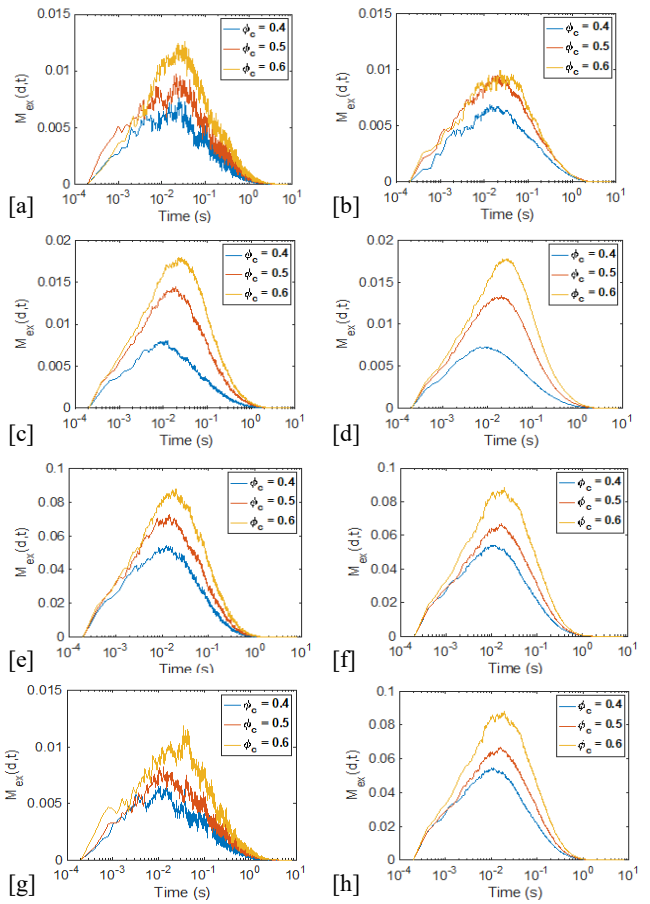

Fig. 11 The magnetization exchange $M_{ex}(d,t)$ as function of observation time for [a, b] pore-filling, [c, d] pore-lining, [e,f] coated, [g, h] laminated samples with clay amount 11 vol% in diffusion direction: left column: macro-micro; right column: micro-macro. Here, the distance is the integration of each EDT shell d = $\sum d.\,\phi_c$ is the micro-porosity for clay phase.

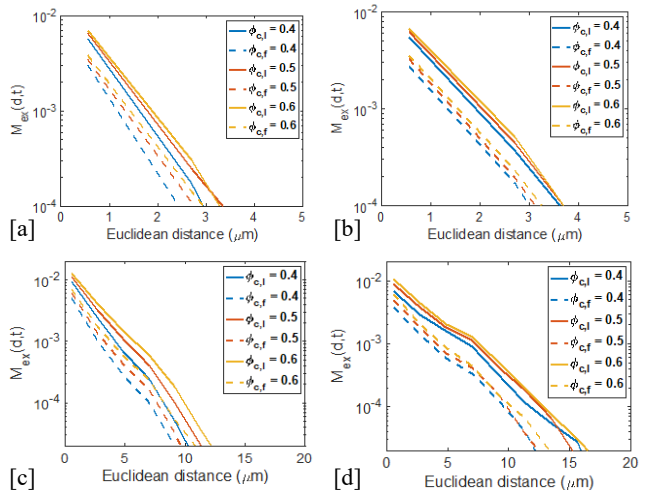

Fig. 12 The magnetization exchange $M_{ex}(d,t)$ of samples with 11 vol% clay from macro- to micro-pore (left column) and from micro- to macro-pore (right column) at various times [a, b] t = 5 t_E; [c, d] t = 50 t_E. The solid line and dash line represent for pore-lining and pore-filling clay distribution respectively.

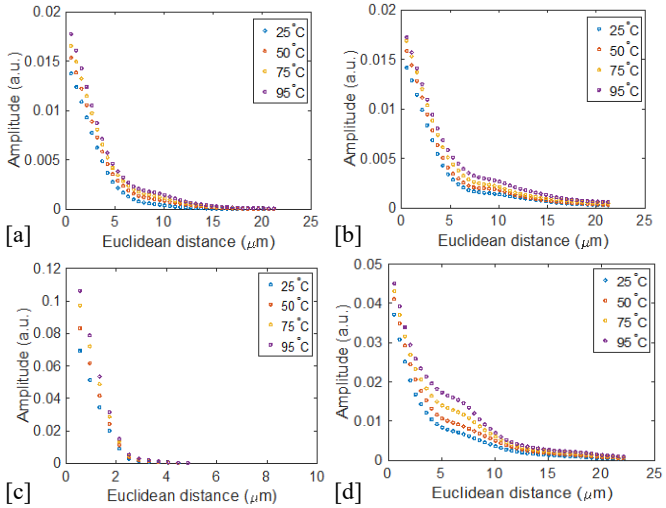

Fig. 13 The correlation of the fitting amplitude at each EDT shell and Euclidean distance in different directions macro-micro (left column) and micro-macro (right column) for [a, b] pore-lining samples, [c, d] coated samples at temperature 25 ℃, 50 ℃, 75 ℃ and 95 ℃.

The corresponding maximum distance at short time (t = 5 t_E) is close to 3-4 μm. The distance increases to 10-15 μm at t = 50 t_E. The higher clay porosity allows more walkers travel to longer distance between micro- and macro-porous regions. The pore-lining sample with lower clay porosity presents less diffusion of magnetization than pore-filling with higher clay porosity. The reason for that may be, that strong surface relaxation is dominant in tight clay pockets. On the contrary, the pore-lining sample always presents higher $M_{ex}(d,t)$ values when walkers travel from micro-pore to macro-pore (Fig. 12b, d).

3.3 Temperature Effects

The diffusional coupling effects can be enhanced with the temperature increasing due to alteration of diffusion coefficient and surface relaxivity [6, 7]. In this section, we noted that we only focus on the contribution of diffusion to magnetization exchange. We simulated the NMR relaxation response at 25 ℃, 50 ℃, 75 ℃ and 95 ℃ with diffusion coefficient $2.15 \times 10^{-5} cm^2/s$, $3.97 \times 10^{-5} cm^2/s$, $6.10 \times 10^{-5} cm^2/s$ and $8.07 \times 10^{-5} cm^2/s$, respectively. The magnetization exchange between micro- and macro-porous regions with integrated time are recorded in respect to particular EDT shell $M_{ex}(d, \sum t)$, that provides the local magnetization evolution in approximate Gaussian distribution. The correlation of the fitting amplitude for $M_{ex}(d, \sum t)$ and Euclidean distance at different temperatures is presented in Fig. 13. Here we demonstrate pore-lining and grain-coated clay morphological types due to their stronger diffusional coupling effects.

As expected, the diffusion of magnetization is enhanced with increased temperature. For pore-lining sample, the diffusion of magnetization becomes weak when distance exceeds 20 μm, the maximum Euclidean distance employed here is 22.05 μm (around 40 voxels) from macro-pore to micro-pore. The amplitude of the magnetization exchange at 95 ℃ is around 1.3 - 1.4 times higher than that at 25 ℃ within the short distance. While, in the opposite direction, the walkers can penetrate slightly deeper into the macro-pore

space. For the grain-coated type, since the distance values around the solid are small, the corresponding penetration distance from macro-pore to micro-pore is around 5 μm. On the contrary, the walkers can still invade macro-pores with distance around 22 μm.

4 Permeability Estimation

In this section, we analyze the coupling effects on permeability estimation for pore-filling and pore-lining samples which are the most common clay patterns in sandstones.

Table 3. The permeability simulated by LBM for pore-lining (K_l) and pore-filling (K_f) samples with different clay amount.

Clay (vol%)	$K_l\ (mD)$	$K_f\ (mD)$
6	639.35	746.41
11	226.59	355.07
16	63.91	109.79

We first calculated permeability by LBM for synthetic clayey sandstones, assuming the clay regions provide no contribution to transport (Table. 3). The permeability values decrease with increasing clay amount. The pore-filling samples exhibit higher permeability than corresponding pore-lining samples of same clay amount. The following analysis of coupling effects on permeability estimate using SDR and Coates models is performed in respect to corresponding prefactors.

4.1 SDR Model

The implications of temperature on the shape of the relaxation time distributions are shown in Fig. 14 [a-f]. We calculated the dimensionless lithological parameter a_s' following Eqn. 2 for both coupling-on and coupling-off scenarios by employing the absolute permeability in Table 3. We report the prefactor $a_{s,l}'$ for pore-lining sample and $a_{s,f}'$ for pore-filling sample with different temperatures in Table 4. The temperature effects are weak when the clay amount is small leading to limited contrast between the coupling-on and coupling-off scenarios. However, as clay amounts increase the temperature effects are enhanced, resulting in a prefactor change of around 1.6 times for the pore-lining sample with clay amount of 16 vol%. While, for pore-filling samples, $a_{s,f}'$ presents weak dependency of temperature due to less shifts and distortion of the T_2 distribution due to diffusion between micro- and macro-porous regions.

4.2 Coates Model

Consider now the permeability estimation via Coates model. According to the coupling-off T_2 distributions (Fig. 15 blue-dashed line), the separated fast relaxation peak corresponds to the bounded irreducible water (S_{wirr}). The normalized BVI is obtained by plotting the cumulative T_2 curves of S_{wirr} in Fig. 15. The $T_{2,cutoff}$ is determined by horizontal projection of S_{wirr} curve for S_w = 100 %. The cross-point is then project down to the x axis with relevant T_2 value, which is $T_{2,cutoff}$ [18]. The correlation between $T_{2,cutoff}$ and temperature for pore-lining and pore-filling samples as function of clay amount is given

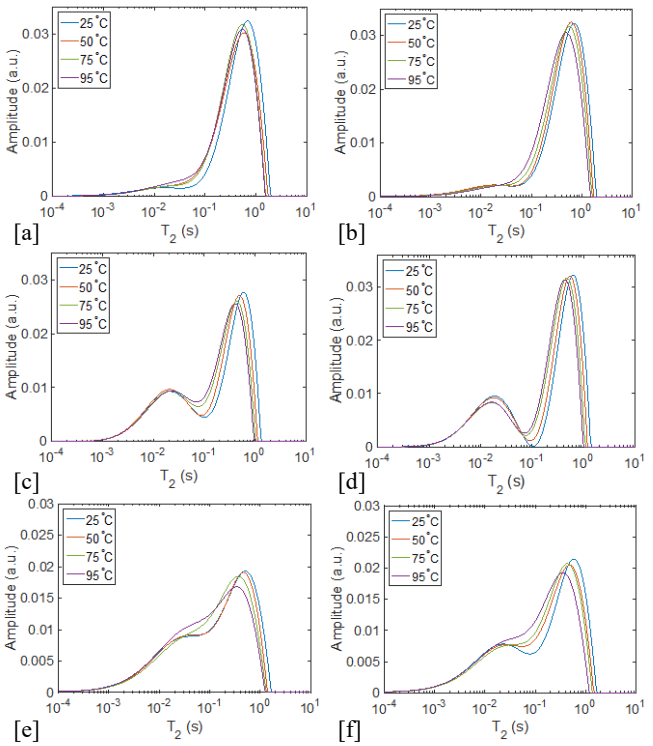

Fig. 14 The comparison of T_2 distributions of pore-lining (left column) and pore-filling (right column) for samples with clay amount [a, b] 6 vol%, [c, d] 11 vol%, [e, f] 16 vol% at the temperature 25 ℃, 50 ℃, 75 ℃ and 95 ℃.

Table 4. The SDR model prefactor for pore-lining sample ($a_{s,l}'$) and pore-filling sample ($a_{s,f}'$) at temperature 25℃, 50℃, 75℃ and 95℃ with different clay amount.

Clay	T	$a_{s,l}'$		$a_{s,f}'$	
(vol)	(℃)	Coupling-on	Coupling-off	Coupling-on	Coupling-off
6	25	1.06	0.94	1.22	1.07
	50	1.34	0.94	1.54	1.09
	75	1.47	0.98	1.67	1.10
	95	1.66	0.98	1.91	1.10
11	25	3.66	1.89	4.36	2.96
	50	5.03	1.94	5.27	3.13
	75	5.39	2.03	5.50	3.16
	95	5.93	2.04	6.39	3.17
16	25	3.97	1.37	6.06	2.28
	50	4.44	1.40	6.47	2.28
	75	4.62	1.41	6.81	2.35
	95	6.51	1.41	7.10	2.37

in Fig 16. The overall trend shows that $T_{2,cutoff}$ values decrease as temperature increase. This may result from the decrease in amplitude of the slow relaxation peak, and the tendency of the bimodal T_2 distribution towards becoming more unimodal with increasing temperature, especially for higher clay amounts (Fig. 14). Since pore-lining clays exhibit stronger

coupling effects, the related $T_{2,cutoff}$ values are lower than for pore-filling clays. As clay amounts increase, the contrast

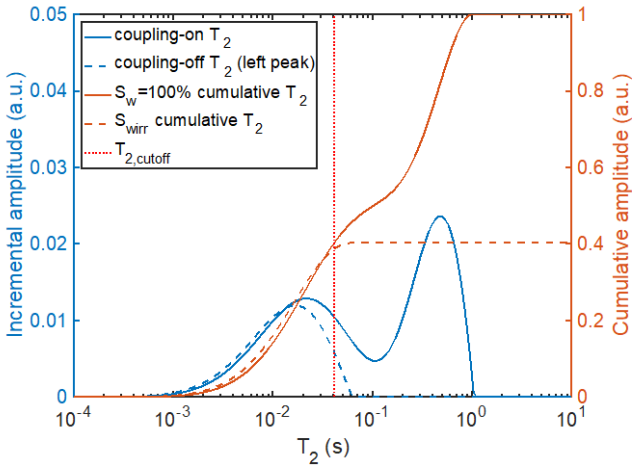

Fig. 15 The cumulative T_2 curves on fully saturated (S_w = 100\%) sample with 11 vol\% clay amount and on irreducible saturation S_{wirr}) are utilized to establish a $T_{2,cutoff}$ via BVI.

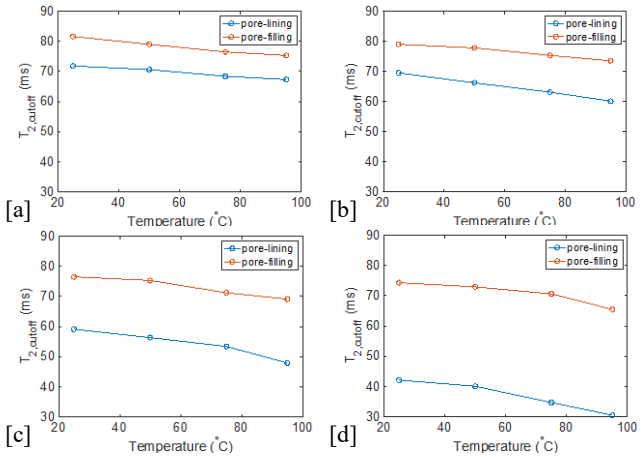

Fig. 16 The correlation between $T_{2,cutoff}$ and temperature for pore-lining and pore-filling samples in different clay amount [a] 2 vol% (original clay amount within Bentheimer sandstone), [b] 6 vol%, [c] 11 vol %, [d] 16 vol%.

Table 5. The Coates model prefactor for pore-lining sample ($a_{c,l}$) and pore-filling sample ($a_{c,f}$) at temperature 25 ℃, 50 ℃, 75 ℃ and 95 ℃ with different clay amount.

Clay (vol%)	T (℃)	$a_{c,l}$	$a_{c,f}$
6	25	10.03	10.09
	50	9.58	10.03
	75	8.85	9.71
	95	8.64	9.59
11	25	45.77	66.55
	50	43.42	63.01
	75	40.59	58.25
	95	36.13	50.73
16	25	92.37	114.82
	50	86.53	107.67
	75	77.39	99.19
	95	72.38	95.14

between the two clay distribution scenarios is growing. When clay amount reaches 16 vol%, the $T_{2,cutoff}$ for pore-lining sample decrease from 42 ms to 30 ms at temperature range from 25 ℃ to 95 ℃. While the reduction for pore-filling samples is from 74 ms to 65 ms.

By applying various $T_{2,cutoff}$, the FFI/BVI ratio can be obtained via T_2 distribution of each sample. With known permeability, porosity and FFI/BVI ratio, we derived prefactor a_c in Coates model according to Eqn. 3. The a_c values are reported in Table 5. The results indicate that the prefactors are not affected much by temperature when little clay is present in the rocks. However, when the clay amount is higher than 10 vol%, both pore-lining and pore-filling samples show dependency on temperature. The smaller $T_{2,cutoff}$ values lead to higher FFI/BVI ratio, resulting in decreased a_c as temperature increasing. Therefore, the permeability may be overestimated if only fixed $T_{2,cutoff}$ is utilized without prefactor compensation.

5 Conclusion

This study evaluates the magnitude of diffusional coupling effects on petrophysical evaluation of clayey sandstone based on NMR transverse relaxation depending on clay volume fraction, distribution pattern, local porosity, and temperatures. The magnetization exchange between micro- and macro-porous regions with aid of EDT map is employed to characterize the diffusion as function of time and penetration depth. This in turn enabled an analysis of potential impacts on permeability predictions. We draw the following specific conclusions:

1. The rocks with coated and pore-lining clay distribution present stronger diffusional coupling effects than pore-filling and laminated one. The distortion of T_2 distribution can result in an overestimation of micro-porosity.
2. The magnetization exchange between micro- and macro-porous regions due to diffusion is demonstrated as exponential function of penetration depth (Euclidean distance) and Gaussian function of observation time.
3. The log-mean of transverse relaxation time demonstrates linear dependency on clay amount. The slope can be altered by different micro-porosity, especially for rocks with pore-lining clay distribution.
4. The diffusional coupling effects are magnified with increasing temperature. The prefactors of SDR model and Coates model exhibit temperature dependency in higher clay amount rocks. The NMR-related permeability can be overestimated if fixed $T_{2,cutoff}$ is utilized without consideration of prefactor compensation.

References

[1] K. Brownstein and C. Tarr, “Importance of classical diffusion in NMR studies of water in biological cells,” *Phys. Rev. A* , vol. 19, p. 446–2453, 1979.

[2] H. Dai, I. Shikhov, R. Li, J. Arns and C. Arns, “Mechanisms of confining pressure dependence of

resistivity index for tight sandstones by digital core analysis," *SPE J.,* vol. 26, p. 883–896, 2021.

[3] S. Apourvari and C. Arns, "Image-based relative permeability upscaling from pore scale," *Adv. Warer Res.,* vol. 95, pp. 161-175, 2016.

[4] J. Qajar, N. Francois and C. Arns, "Microtomographic characterization of dissolution-induced local porosity changes including fines migration in carbonate rock," *SPE J.,* vol. 18, p. 545–562, 2013.

[5] E. Grunewald and R. Knight, "A laboratory study of NMR relaxation times and pore coupling in heterogeneous media," *Geophysics ,* vol. 74, p. 215–221, 2009.

[6] V. Anand and G. Hirasaki, "Paramagnetic relaxation in sandstones: distinguishing *T*1 and *T*2 dependence on surface relaxation, internal gradients and dependence on echo spacing," *J. Magn. Reson,* vol. 190, p. 68 – 85, 2008.

[7] E. Toumelin, C. Torres-Verdin, S. Chen and D. Fischer, "Analysis of NMR diffusion coupling effects in two-phase carbonate rocks: comparison of measurements with Monte Carlo simulations," in *SPWLA 43rd Annual Logging Symposium*, Oiso, Japan, 2002.

[8] E. Toumelin, C. Torres-Verdín, S. Chen and D. Fischer, "Reconciling NMR measurements and numerical simulations: assessment of temperature and diffusive coupling effects on two-phase carbonate samples," *Petrophysics,* vol. 44, 2003.

[9] N. Gomaa, A. Al-Alyak, D. Ouzzane, O. Saif, M. Okuyiga, A. Opco, D. Allen, D. Rose, R. Ramamoorthy and E. Bize, "Case study of permeability, Vug quantification, and rock typing in a complex carbonate," in *SPE Annual Technical Conference and Exhibition*, San Antonio,Texas, 2006.

[10] W. Trevizan, P. Netto, B. Coutinho, V. Machado, E. Rios, S. Chen, W. Shao and P. Romero, "Method for predicting permeability of complex carbonate reservoirs using NMR logging measurements," *Petrophysics,* vol. 55, p. 240–252, 2014.

[11] M. Fleury and J. Soualem, "Quantitative analysis of diffusional pore coupling from T_2-store-T_2 NMR experiments," *Journal of Colloid and Interface Science,* vol. 336, p. 250–259, 2009.

[12] C. Morriss, J. Maclnnis, R. Freedman, J. Smaardyk, C. Straley, W. Kenyon, H. Vinegar and P. Tutunjian, "Field test of an experimental pulsed nuclear magnetism tool," in *SPWLA 34th Annual Logging Symposium*, Calgary, Alberta, 1993.

[13] C. Straley, D. Rossini, P. Tutunjian, H. Vinegar and C. Morriss, "Core analysis by low-field NMR," in *The Log Analyst 38*, 1997.

[14] G. Coates, J. Galford, D. Mardon and D. Marschall, "A new characterization of bulk-volume irreducible using magnetic resonance," in *The Log Analyst 39*, 1998.

[15] E. Toumelin, C. Torres-Verdín and S. Chen, "Modeling of multiple echo-time NMR measurements for complex pore geometries and multiphase saturations," *SPE Reser. Eval. Eng.,* vol. 6, p. 234–243, 2003.

[16] S. Godefroy, M. Fleury, F. Deflandre and J. Korb, "Temperature effect on NMR surface relaxation in rocks for well logging applications," *J. Phys. Chem. B,* vol. 106, p. 11183–11190, 2002.

[17] E. Kenyon, I. Day, C. Straley and F. Willemsen, " A three-part study of NMR longitudinal relaxation properties of water-saturated sandstones," *SPE Formation Evaluation,* vol. 3, p. 622–636, 1988.

[18] G. Coates, L. Xiao and M. Prammer, NMR logging: principles and applications, Houston: Haliburton Energy Services, 1999.

[19] G. Carneiro, A. Souza, A. Boyd, L. Schwartz, Y. Song, R. Azeredo, W. Trevizan, B. Santos, E. Rios and V. Machado, "Evaluating Pore Space Connectivity by NMR Diffusive Coupling," in *SPWLA 55th Annual Logging Symposium*, Abu Dhabi, United Arab Emirates, 2014.

[20] M. Jácomo, R. Trindade, E. de Oliveira, C. Leite, E. Montrazi, M. Andreeta and T. Bonagamba, "Nuclear magnetic resonance and pore coupling in clay-coated sandstones with anomalous porosity preservation, ÿgua Grande Formation, Rec & ocirc;ncavo Basin, Brazil," *Petrophysics ,* vol. 59, p. 136–152, 2018.

[21] S. Chen, D. Jacobi, H. Kwak, M. Altunbay and J. Kloos, "Pore-connectivity based permeability model for complex carbonate formations," in *SPWLA 49th Annual Logging Symposium*, ustin, Texas, 2008.

[22] L. Chi and Z. Heidari, "Directional-permeability assessment in formations with complex pore geometry with a new nuclear-magnetic-resonance-based permeability model," *SPE J.,* vol. 21, p. 1436–1449, 2016.

[23] M. Cohen and K. Mendelson, "Nuclear magnetic relaxation and the internal geometry of sedimentary rocks," *J. Appl. Phys.,* vol. 53, p. 1127–1135, 1982.

[24] T. Ramakrishnan, E. Fordham, W. Kenyon, L. Schwartz and D. Wilkinson, "Forward models for nuclear magnetic resonance in carbonate rocks," in *The Log Analyst 40*, 1999.

[25] Z. Zhang, D. Johnson and L. Schwartz, "Simulating the time-dependent diffusion coefficient in mixed-pore-size materials," *Phys. Rev. E,* vol. 84, p. 031129, 2011.

[26] L. Schwartz, D. Johnson, J. Mitchell, T. Chandrasekera and E. Fordham, "Modeling two-dimensional magnetic resonance measurements in coupled pore systems," *Phys. Rev. E,* vol. 88, p. 032813, 2013.

[27] J. Mitchell, A. Souza, E. Fordham and A. Boyd, "A finite element approach to forward modeling of nuclear magnetic resonance measurements in coupled pore systems," *J. Chem. Phys.,* vol. 150, p. 154708:1–12, 2019.

[28] C. Arns, A. Sheppard, R. Sok and M. Knackstedt, "NMR petrophysical predictions on digitized core

images," in *46th Annual Logging Symposium, Society of Petrophysicists & Well Log Analyst*, New Orleans, Texas, 2005.

[29] L. Chi and Z. Heidari, "Diffusional coupling between microfractures and pore structure and its impact on nuclear magnetic resonance measurements in multiple-porosity system," *Geophysic,* vol. 80, pp. 31-42, 2014.

[30] C. Arns, Y. Melean, A. Sheppard and M. Knackstedt, "A comparison of pore structure analysis by NMR and Xray-CT techniques," in *9th Annual Logging Symposium, Society of Petrophysicists & Well Log Analyst*, Edinburgh, 2008.

[31] M. Tankiewicz, "Experimental Investigation of Strength Anisotropy of Varved Clay," *Procedia Earth Planet. Sci.,* vol. 15, p. 732–737, 2015.

[32] Y. Cui, I. Shikhov and C. Arns, "NMR relaxation modeling in porous media with dual-scale resolved internal magnetic fields," *Transport in Porous Media,* 2022.

[33] A. Sheppard, R. Sok and H. Averdunk, "Techniques for image enhancement and segmentation of tomographic images of porous materials," *Physica A ,* vol. 339, p. 145–151, 2004.

[34] T. Saito and J. Toriwaki, "New algorithms for Euclidean distance transformation of an n-dimensional digitized picture with applications," *Pattern Recognition ,* vol. 27, p. 1551–1565, 1994.

[35] C. Arns, A. Sakellariou, T. Senden, A. Sheppard, R. Sok, W. Pinczewski and M. Knackstedt, "Digital core laboratory: Reservoir core analysis from 3D images," *Petrophysics,* vol. 46, no. 260–277, 2005.

[36] Y. Cui, I. Shikhov, R. Li, S. Liu and C. Arns, "A numerical study of field strength and clay morphology impact on NMR transverse relaxation in sandstones," *J. Pet. Sci. Eng,* vol. 202, p. 10852, 2021.

[37] J. Mbey, F. Thomas, A. Razafitianamaharavo, C. Caillet and F. Villiéras., "A comparative study of some kaolinites surface properties," *Applied Clay Science,* vol. 172, p. 135–145, 2019.

[38] A. Matteson, J. Tomanic, M. Herron, D. Allen and W. Kenyon, "NMR relaxation of clay-brine mixtures," *PE Reser. Eval. Eng. ,* vol. 3, p. 408–413, 2000.

[39] Y. Zheng, I. Shikhov, L. Gbayan, J. Arns and C. Arns, "About the connectivity of dual-scale media based on micro-structure based regional analysis of NMR flow propagators," *J. Contam. Hydrol.,* vol. 212, p. 143–151, 2018.

[40] D. Bergman, K. Dunn, L. Schwartz and P. Mitra, "Self-diffusion in a periodic Porous medium: a comparison of different approaches," *Phys. Rev. E,* vol. 51, p. 3393–3400, 1995.

[41] A. Katz and A. Thompson, "Quantitative prediction of permeability in porous rock," *Phys. Rev. B ,* vol. 34, p. 8179–8181, 1986.

[42] L. Johnson, J. Koplik and L. Schwartz, "New pore size parameter characterizing transport in porous media," *Phys. Rev. Lett. ,* vol. 57 , p. 2564–2567, 1986.

[43] J. Banavar and L. Schwartz, "Magnetic resonance as a probe of permeability in porous media," *Phys. Rev. Lett.,* vol. 58, p. 1411–1414, 1987.

[44] U. Frisch, B. Hasslacher and Y. Pomeau, "Lattice-gas automata for the Navier-Stokes equation," *Phys. Rev. Lett. ,* vol. 56, p. 1505–1508, 1986.

[45] D. Rothman, "Cellular-automaton fluids: A model for flow in porous media," *Geophysics ,* vol. 53, p. 509–518, 1988.

[46] B. Ferreol and D. Rothman, "Lattice-Boltzmann simulations of flow through Fontainebleau sandstone," *Trans. Porous. Med.,* vol. 20, p. 3–20, 1995.

[47] N. Martys and J. Hagedorn, "Multiscale modeling of fluid transport in heterogeneous materials using discrete boltzmann methods," *Materials and structures,* vol. 35, p. 650–658, 2002.

[48] N. Martys and H. Chen, "Simulation of multicomponent fluids in complex three-dimensional geometries by the lattice Boltzmann method," *Phys. Rev. E,* vol. 53, p. 743–750, 1996.

[49] M. Elsayed, G. Glatz, A. El-Husseiny, A. Alqubalee, A. Adebayo, K. Al-Garadi and M. Mahmoud, "The effect of clay content on the spin–spin NMR relaxation time measured in porous media," *ACS Omega,* vol. 5, p. 6545–6555, 2020.

[50] D. Johnson and L. Schwartz, "Analytic theory of two-dimensional NMR in systems with coupled macro- and micropores," *Phys. Rev. E ,* vol. 90, p. 032407, 2014.